Soft Matter

Cohesive and adhesive properties of crosslinked semiflexible biopolymer networks

Journal:	*Soft Matter*
Manuscript ID	SM-ART-11-2018-002277.R2
Article Type:	Paper
Date Submitted by the Author:	31-Mar-2019
Complete List of Authors:	Zhang, Yao; Northwestern University, Mechanical Engineering DeBenedictis, Elizabeth; Northwestern University, ; Keten, Sinan; Northwestern University, Mechanical Engineering

Cohesive and adhesive properties of crosslinked semiflexible biopolymer networks

Yao Zhang[1], Elizabeth P. DeBenedictis[1], Sinan Keten[1,2,*]

[1]Department of Mechanical Engineering, Northwestern University, Evanston, Illinois 60208, United States

[2]Department of Civil and Environmental Engineering, Northwestern University, Evanston, IL 60208, United States

[*] Corresponding author

E-mail: s-keten@northwestern.edu

Abstract

Biomolecular semiflexible polymer networks with persistence lengths well above those of single polymeric chains serve important structural and adhesive roles in biology, biomaterials, food science and many other fields. While relationships between the structure and viscoelasticity of semiflexible polymer networks have been previously investigated, it remains challenging to systematically relate fibril and network properties to cohesive and adhesive properties that govern the function of these materials. To address this issue, here we utilize coarse-grained molecular dynamics simulations to thoroughly elucidate how the work of adhesion of a semiflexible polymer network to a surface depends on crosslink density and fibril persistence length. Two emergent characteristics of the network are its elasticity and its interfacial energy with the surface. Stiff networks that are either highly crosslinked or have high persistence length fibrils tend to have lower interfacial energy, and consequently, lower work of adhesion. For lightly crosslinked networks with flexible fibrils, considerable strain energy must be stored within the adhesive during detachment, which creates an additional penalty to detachment. Increasing persistence length while keeping crosslink density constant leads to porous, low density networks, leading to an optimal fibril persistence length at which maximum work of adhesion per mass density is attained for a given crosslink density. For any given fibril persistence length, increasing crosslink density has a slightly negative effect on network mass density and interfacial energy. A critical crosslink density is found, below which the networks have no significant load-bearing capacity. Lightly crosslinked networks above this threshold absorb more strain energy during desorption and consequently possess greater work of adhesion. The conflict between mass density and stiffness results in non-

monotonic trend between the ratio of work of adhesion to interfacial energy and persistence length. These findings provide physical insight into the adhesive mechanisms of biomaterials based on crosslinked semiflexible polymer networks, and reveal important design guidelines for bio-adhesives.

Introduction

Semiflexible biopolymers are ubiquitous in nature, ranging from amyloid fibrils in bacterial biofilms to actin filaments in cells. As natural protein materials, nanoscale semiflexible fibrils possess substantial stiffness and bending rigidity (*e.g.*, Young's moduli of approximately 0.2-20 and 3 GPa for amyloid fibrils[1-4] and actin filaments[5], respectively), which is difficult to replicate in synthesized fibers. The persistence length of a polymer chain is typically less than a nanometer, while the persistence lengths of semiflexible biopolymers often exceed tens of nanometers and can be in the micron range, as in the case of amyloid fibrils[3]. To serve biological functions, semiflexible biopolymers typically self-assemble into three-dimensional fibrous networks. Cellular cytoskeletons made up of actin filaments, intermediate filaments, and microtubules[6], extracellular matrices made up of collagen fibers, elastins, fibronectins, and laminins[7], and bacterial biofilms consisting of amyloid fibrils, eDNA, and polysaccharides[8] are notable examples of network biomaterials.

These semiflexible biopolymer networks with hierarchical structures at different length scales (*i.e.* monomer, fibril and network scales) provide mechanical stability to biological systems and play important roles in cellular morphology, mobility, and adhesion[9-11]. In particular, semiflexible amyloid fibrils are one of the main adhesive and structural components of bacterial biofilms[12-17], whose strong adhesion to various abiotic and biotic surfaces presents significant challenges in medical, food, and marine industries, and is still poorly understood. Studying semiflexible biopolymers networks is vital to understand fundamental biological functions such as biofilm formation, but also has become relevant for novel materials fabrication. For example, recent advances in utilizing genetically modified *Escherichia coli* to produce curli amyloid fibril networks with tunable functions, such as enhanced adhesion and conductivity, opens up new avenues for the application of semiflexible biopolymer networks as multi-functional materials[18-21]. A deeper understanding of the properties of semiflexible biopolymer networks is needed to further their potential applications as adhesives, structural materials, and biomaterials[18, 22].

Strong biocompatible adhesives are highly sought after in biomedical applications, such as tissue repair and wound dressing[23, 24], and bioinspired adhesives have been studied extensively[25-30].

Inspired by the strong adhesion of bacterial biofilms to various surfaces, semiflexible biopolymer networks, formed by amyloid fibrils or similar nanofibrous components, are emerging as promising bio-adhesives[18]. Although the adhesion mechanisms of amyloids to surfaces at the monomer and fibril scale and the adhesion between fibers within networks have recently been investigated[31-36], the adhesion mechanisms to surfaces at the network scale remain unexplored. Recent studies have suggested that the adhesive performance of fibril networks not only depends on the surface chemistry at the interface but is also dictated by the network structure and mechanical properties[24, 37]. For instance, heterogeneous material distribution has a crucial influence on the impact tolerance of mussel thread networks adhered to substrates[37]. For amyloid fibril networks, it is unknown how the density/pore size and constituent fibril stiffness influence mechanical and adhesive properties. Studying the cohesive and adhesive properties of crosslinked semiflexible biopolymer networks is needed to understand the structure-property relationship of biofilm matrices and could pave the way for the design of amyloid fibril based adhesives.

It is impossible to study the adhesive performance of networks without taking their mechanical behavior into account, since deformation and dissipation within the network contributes to the work of adhesion. Considerable effort has been devoted to describing the constitutive behavior of semiflexible biopolymer networks. Crosslinked actin filament, collagen, and fibrin networks have been reconstituted from purified monomers and the dependence of their elastic moduli on biopolymer concentration, crosslink density, strain, and stress has been experimentally characterized[38-41]. Complementary to these experimental studies, theoretical analyses incorporating tension-extension relationships of polymer segments under thermal fluctuations have been proposed to establish constitutive laws for crosslinked biopolymer networks, as well as scaling laws that relate their elastic moduli to biopolymer concentration or crosslink density[40-44]. The disordered nature of networks and the scales involved pose challenges to experimental characterization of biopolymer networks, but present an opportunity for bottom-up simulations. Previously, the finite element method was used to study the effect of filament bending and stretching stiffness, filament length, and crosslink connectivity on the stress-strain responses of three-dimensional crosslinked networks of actin filaments[45], as well as the strength and mechanical behaviors of crosslinked fiber networks[46, 47]. A Monte Carlo approach involving beads connected with worm-like chains was used to investigate the influence of the length of biopolymer segment

between crosslinks, biopolymer persistence length, and shear strain on stiffening and nonaffine behavior of crosslinked semiflexible biopolymer networks subjected to shear strains[48]. Similar models of crosslinked semiflexible polymer networks have been used to investigate their frequency-dependent stiffening, internal stresses, normal modes, and nonaffinity[49, 50]. Coarse-grained molecular dynamics and Brownian dynamics models, in which polymer chains are represented by bead spring models, have also been used to investigate the structures and dynamic moduli of crosslinked actin filament network[51, 52]. So far, computational studies of crosslinked semiflexible polymer networks have not considered the failure of semiflexible polymers. Furthermore, the effect of crosslink density, especially in the low crosslink density regime, has not been systematically explored, to our knowledge. Most importantly, previous theories, experiments and simulations have primarily focused on the viscoelasticity of semiflexible biopolymer networks but understanding of their adhesive properties remains lacking.

A challenge to be addressed for studying amyloid based networks is to account for mechanisms such as monomer unfolding, fibril sliding, and crosslink formation and breaking (physical and/or chemical), as well as bending induced breaking or fragmentation of fibrils. The ultimate goal is to create generic models that can simultaneously capture these mechanisms as they apply to different systems. A good starting point towards that capability is to look at systems where fibrils have minimal cohesive interactions, considerable high bending rigidity, and crosslinks representing interfibril interactions in a general sense. Coarse-grained molecular dynamics is a suitable choice that offers a good balance between discrete molecular-scale resolution and computational efficiency[53-57]. In this context, this work aims to uncover how network structure and constituent semiflexible fibril properties affect mechanical and adhesive properties of chemically crosslinked networks. A coarse-grained three-dimensional network model with tunable crosslink density and fibril mechanical properties is developed, which accounts for fibril failure. This coarse-grained model was used to study the effect of crosslink density and fibril persistence length on network mechanical and adhesive properties. We first introduce the semiflexible fibril model, and how this is used to generate a three-dimensional crosslinked network. We then allow the networks to adsorb onto a surface and apply tensile force to study the influence of network parameters (*i.e.* persistence length and crosslink density) on the work of adhesion of the semiflexible network.

Methods

Semiflexible biopolymer model

A bead spring model, an extensively used coarse-grained approach to describe polymer chains, is employed to model semiflexible biopolymers in this study. The parameters used in developing this model were selected to approximate the curli fiber network structure and mechanics. As shown in Figure 1a, the semiflexible biopolymer is modeled as coarse-grained beads connected by harmonic bonds. Angle potentials are defined among every 3 neighboring beads to provide the bending rigidity of the polymer. As the coarse-grained polymer's Young's modulus and bending rigidity are governed by bond and angle terms, respectively, bead spring models can decouple the two mechanical properties. The bond potential is given by

$$V_S(r) = \frac{1}{2}k\left(r - r_0\right)^2, \qquad (1)$$

where r is the distance between two bonded beads, k is the spring constant, and r_0 is the equilibrium bond length. The relationship between the spring constant k and Young' modulus of the semiflexible polymer is $k = \frac{AE}{r_0}$, where E is Young's modulus and A is the cross-sectional area of the fibril. Here, the semiflexible fibril is taken to be representative of the properties of a curli amyloid fibril. Based on the backbone dimensions of curli monomers, r_0 and A are set as 2 nm and 3.1 nm^2, respectively[58]. The spring constant k is then chosen as k=10k_BT/Å^2, and the resultant fibril Young's modulus E=2.6 GPa matches well with the Young's modulus of amyloid fibrils measured from AFM experiments[2].

The angle potential is chosen such that it can directly control the bending rigidity. The bending energy of a polymer chain is $E_B = \frac{\kappa}{2}\int_0^l C^2 ds = \frac{\kappa}{2}\int_0^l \left|\frac{\mathbf{T}}{s}\right|^2 ds$, where κ is the bending rigidity of the polymer, C is the local curvature, l is the contour length, and $\mathbf{T}$ is the unit tangent vector. In our bead spring model shown in Figure 1a, the bending energy is

$$E_B = \frac{\kappa}{2}\int_0^l \left|\frac{\mathbf{T}}{s}\right|^2 ds \approx \frac{\kappa}{2} r_0 \sum_i \left(\frac{\mathbf{T}_{i+1} - \mathbf{T}_i}{r_0}\right)^2 = \frac{\kappa}{r_0}\sum_i \left(1 - \cos(\pi - \theta_i)\right), \quad (2)$$

where θ is the angle. Here the angle potential is chosen as

$$V_B(\theta) = \frac{\kappa}{r_0}(1-\cos(\pi-\theta)),\ (0<\theta<2\pi) \quad (3)$$

so that fibril bending rigidity can be directly tuned by varying constants in the angle potential. To test this relationship, we compare the assigned bending rigidity in the angle potential and the resulting bending rigidity of the coarse-grained semiflexible polymer chains calculated from thermally induced shape fluctuations in molecular dynamics simulations. Briefly, one end of a coarse-grained semiflexible polymer chain is clamped, and the thermally induced fluctuation of the other end is monitored and used to calculate bending rigidity with the equation:

$$\kappa = \frac{k_B T L^3}{3\left\langle \delta u(L)^2 \right\rangle}, \quad (4)$$

where L is the length of the semiflexible polymer chain and $\delta u(L) = u(L) - \langle u(L) \rangle$ is the deviation of the free end from its average position[32, 59]. Curli can grow to variable length up to micrometers long, and the polymer chains here are taken to be 600 nm in length. When $\kappa = 1\times10^{-25}\ N\cdot m^2$ is used in the angle potential, the resulting bending rigidity of single coarse-grained polymer is $\kappa = 1.46\pm1.80\times10^{-25}\ N\cdot m^2$. Despite the inherently large variation in measured bending rigidity using thermally induced shape fluctuations, the assigned and resulting bending rigidity actually match well. In this work, as we focus on the effect of biopolymer bending rigidity on network properties, we fix the Young's modulus of the biopolymer and tune the bending rigidity across a wide range of values. Since persistence length ($l_p = \frac{\kappa}{k_B T}$) is linearly proportional to bending rigidity, tuning the persistence length is the same as tuning the bending rigidity. The persistence lengths tested in this study vary from 0.001 μm to 243.8 μm, a range whose span includes experimentally measured values[2, 60, 61].

Generation of crosslinked networks

To extend the coarse-grained semiflexible fibril model to coarse-grained network structures, we have developed a two-step coarse-graining modeling method to generate a crosslinked network of semiflexible fibrils. The first step is to generate randomly distributed semiflexible fibrils. In this step, 900 coarse-grained fibrils with a contour length of 600 *nm* were placed in a 700nm×700nm×700nm periodic simulation box. Each coarse-grained fibril is a chain of 300 beads

connected by harmonic bonds with an equilibrium distance of 2 nm. The interaction between beads from different fibrils is described by a Lennard-Jones potential:

$$V_R(r) = \varepsilon_1\left[\left(\frac{r_m}{r}\right)^{12} - 2\left(\frac{r_m}{r}\right)^{6}\right], \quad (5)$$

where r_m=$2^{1/6}\sigma$ (σ=2 *nm*) and ε_1=0.01 k_BT. This potential provides a steric repulsion force between beads from different fibrils at short distances with a cut-off distance of 2.5σ. Within one fibril, this potential is also applied to beads that are not directly connected by harmonic bonds. To obtain randomly distributed fibrils, the temperature of the system was heated to 600K, maintained at that temperature and then cooled down to room temperature (300K) in the NVT ensemble. The timestep of all the simulations are fixed at 0.15 ps, and 1 million steps (150 ns) are run to generate randomly distributed polymer chains. The second step is to add crosslinks between randomly distributed polymer chains to form crosslinked networks in the NVT ensemble. As shown in Figure 1b, each coarse-grained polymer chain has 7 potential crosslink beads represented by the blue beads in the chain. The 7 beads evenly divide the chain into 6 short segments with a length of 100 *nm*. In this step, the Lennard-Jones potential is temporarily applied to all potential crosslink beads as

$$V_A(r) = \varepsilon_2\left[\left(\frac{r_m}{r}\right)^{12} - 2\left(\frac{r_m}{r}\right)^{6}\right], \quad (6)$$

where r_m=$2^{1/6}\sigma$ (σ=2 *nm*), its energy well depth ε_2 is set as $2k_BT$, and its cut-off distance is 2.5σ. When two potential crosslink beads are within around 2 *nm*, a harmonic bond is created to model chemical crosslinking and the Lennard-Jones potential between those two bonded beads is turned off. After all crosslinks are generated, this potential is removed and beads from different fibril or non-neighboring beads in the same fibril only have a steric repulsion force given by the potential in equation (5). The total number of crosslinks first increases with the simulation time and then saturates at a maximum number. The bond potential is the same as the potential shown in equation (1). The crosslink density and connectivity of semiflexible polymer networks has been shown to influence elasticity[38, 62, 63]. One potential crosslink bead is not allowed to bond with two or more other potential crosslink beads. The resulting crosslinks are four-way junctions (i.e., crosslink between two non-end beads), three-way junctions (i.e., crosslink between a non-end bead and end

bead), and two-way junctions (i.e., crosslink between two end beads). As end beads are only two of seven potential crosslink sites, the majority of crosslinks are three-way or four-way, with less than 14% represented by two-way junctions. When a targeted crosslink density is reached, the applied Lennard-Jones potential is turned off for all the beads. To check whether the orientation of polymer chains in the network is randomly distributed, Herman's orientation parameters with respect to x, y and z axes are examined for 6 different networks. The 6 different networks refer to networks with a persistence length of 2.44 μm and various crosslink densities (n=1.56, 2.39, 3.39, 4.50, 5.47), which are also used to investigate the effect of crosslink density in the results section. The crosslink density is quantified by the number of crosslinks per fibril (n), which is given by $n = \frac{2N_c}{N_f}$ (N_c is the total number of crosslinks and N_f=900 is the total number of fibrils). The range of crosslink densities is selected such that the mean distance between fiber intersections is within the range of curli networks (tens to hundreds of nm), as observed in experimental images[64-66]. For these 6 networks (Fig. 1c), the Herman's orientation parameters with x, y and z axes are 0.048±0.004, 0.036±0.006 and 0.089±0.009, respectively. These values (close to zero) indicate a random distribution of fibril orientations in the network, which should result in isotropic behavior.

Fibril failure criterion

In our model, the possibility of bond rupture along the semiflexible fibril is also considered. We set the failure strain of coarse-grained fibril at 0.125 loosely based on recent computational study where it was found that amyloid fibrils fail at a strain around 0.1−0.15[67], When the harmonic bond length between coarse-grained beads is larger than 1.125 r_0, the harmonic bond and the associated angle between the three beads will be deleted in the simulation. In this case, the energy cost to break a bond is about 31.25 k_BT. The crosslinks are also allowed to fail when bond length increases to the 1.125 times of equilibrium length in the present model. The bond-breaking criterion of crosslinks is the same as that of the semiflexible fibrils. The bond energy of crosslinks is also 31.25 k_BT, which was chosen to represent a value between the bond energy of a hydrogen bond and of a covalent bond.

Measurement of work of adhesion

Using the developed network model, we investigate the adhesive performance of crosslinked semiflexible networks by examining their work of adhesion, defined by the total work to detach the network from a surface. To calculate the work of adhesion, equilibrium networks are placed on the surface and are then allowed to fully adsorb on the surface as shown in Figure 2a. The surface is modeled as a 2D square lattice with a side length of 1.3 *nm*. Each coarse-grained bead in the network has non-specific interactions with beads on the surface, described as

$$V_{Adhesion}(r) = \varepsilon_A \left[\left(\frac{r_m}{r} \right)^{12} - 2 \left(\frac{r_m}{r} \right)^{6} \right], \quad (7)$$

Where $r_m = 2^{1/6}\sigma$ (σ=2 *nm*) and ε_A is the adhesive strength between the network and surface beads. The cut-off distance of the potential is set as 2.5σ. The total adhesion energy of a coarse-grained bead in a fibril to the surface is 8.74 ε_A. This is defined by the energy minimum of the potential between a single bead and the surface, indicating the strength of attraction between the two. The intermolecular potential between fibril beads and the substrate was chosen based on a previous atomistic study of curli subunits on polar and nonpolar surfaces[31]. Steered molecular dynamics (SMD) simulations are then performed using NVT ensemble in LAMMPS[68] to detach the network from the surface along the z direction (normal to the network-surface interface) with a pulling velocity of 1.4 *nm*/*ns*. The timestep and Tdamp of all the simulations are set as 0.15 ps and 150 ps, respectively. In the SMD simulations, the beads within a very thin layer on top of the network (marked by a grey color in Figure 2a with a thickness of ~40 nm) are tethered by the steering force *f* zto a virtual atom through a virtual spring. The work of adhesion of the network is the total work to detach the network, which is determined by the potential of mean force (PMF) obtained from SMD. We have tested different pulling velocities (i.e., 2.8 nm/ns, 1.4 nm/ns, and 0.7 nm/ns). Simulation results show that the work of adhesion obtained from SMD are almost the same (the difference is less than 3.2%) when the pulling velocity is lower than 2.8 nm/ns as shown in the Figure S1. To reduce computational cost, we chose 1.4 nm/ns as the pulling velocity.

Results

To investigate the adhesion of semiflexible networks, we allow the networks to fully adsorb onto a surface and apply a steering force to study the influence of persistence length and crosslink density on their work of adhesion. When increasing the adhesive strength (ε_A) while keeping fibril persistence length (l_p=2.44 μm) and crosslink density (n=4.5) constant, both adhesive failure

(Figure 2b) and cohesive failure (Figure 2c) can be observed during the detachment of networks from surfaces. As the adhesive strength (ε_A) increases, the work of adhesion first increases predictably in the adhesive failure regime and then decreases in the cohesive failure regime (Figure 2d). Gradual desorption of fibrils from the surface leads to the adhesive failure in low adhesive strength range ($\varepsilon_A < 2.5\ k_BT$), while rupture of fibrils leads to the cohesive failure in high adhesive strength range ($\varepsilon_A \geq 2.5\ k_BT$). To investigate the effect of fibril persistence length and crosslink density on network adhesion, we focus on the adhesive failure regime and set the adhesive strength as $\varepsilon_A = 1 k_BT$. In this case, the adhesion energy between the surface and one coarse-grained monomer is 8.74 k_BT.

We first look at the effect of fibril persistence length on the work of adhesion. In this case, the crosslink density remains the same, but the polymer persistence length is varied from 0.001 μm to 243.8 μm. The adhesive strength is $\varepsilon_A = 1\ k_BT$. The interfacial energy (γ_A) between the network and the surface first increases and then saturates as the fibril persistence length decreases (Figure 3a). Since the interfacial energy (γ_A) is the summation of potential energy between network beads and surface beads, a larger interfacial energy means more fibrils contact the surface. As the fibril persistence length decreases, the network becomes more flexible (Figure S2a) and more fibrils contact the surface during adsorption until reaching the maximum fibril density allowed on the surface. The work of adhesion (γ_T) first increases with decreasing fibril persistence length, and then saturates in the small persistence length range ($l_p \leq 0.12$ μm) as shown in Figure 3c. On the other hand, decreasing persistence length also leads to a dramatic increase in the network mass density (the total mass of fibrils per unit volume), especially when persistence length is smaller than 0.24 μm (Figure S2b). It should be noted that the mass density is measured when the network is in equilibrium without the surface present. The change in mass density is attributed to the change in the ratio of mean end-to-end distance ($\bar{L}_e$) to the corresponding mean contour length ($\bar{L}_c$) of fibril segments in networks, which greatly decreases with decreasing fibril persistence length in the regime $l_p \leq 0.24$ μm (Figure S2c). Networks with strong adhesion but lower mass are desirable where weight is a consideration. Networks with less mass density also possess larger pore size, which may be advantageous for other purposes, for instance, to facilitate mass transport through the network in biological systems, such as biofilms. To account for the network mass density

effects, the network work of adhesion and the interfacial energy are normalized by the volume fraction of polymer chains (ϕ_p) in the network, which is dimensionless and linearly proportional to the network mass density. Figure 4 shows that both normalized work of adhesion ($\gamma_T/\phi_p^{2/3}$) and interfacial energy ($\gamma_A/\phi_p^{2/3}$) first increase, reach maximum values at l_p=0.12~0.24 μm and then decrease, as the fibril persistence length increases. Interestingly, the work of adhesion (γ_T) is much larger than the interfacial energy (γ_A) as shown in Figure 3 a and c. This suggests that other energy costs also contribute to the work of adhesion. Figure S2a plots the stress-strain curves of networks with different polymer persistence lengths during desorption. We can see that the network with a shorter fibril persistence length has a lower Young's modulus (the slope of stress-strain curve in the small strain range) and absorbs more strain energy per volume (the area under stress-strain curve). Figure 3b shows that the absorbed strain energy (γ_C, total strain energy normalized by the interfacial area between the surface and the network) by the network increases with decreasing fibril persistence length until it reaches a maximum value at l_p=0.02 μm. The fact that γ_C is very close to γ_T-γ_A indicates that the difference between interfacial energy and work of adhesion is mainly attributed to differences in strain energy stored in the deformed network during the desorption process. In contrast, the work of adhesion of a glassy polymer on a substrate is very close to the interfacial energy[69]. A glassy polymer with a Young's modulus on the order of GPa is too stiff to deform and store significant strain energy during desorption.

To better understand the dependency of interfacial energy, absorbed strain energy, and work of adhesion on the persistence length, a simple model is developed. When l_p is less than 0.244 μm, the network is soft and network coverage on the surface reaches a maximum value. Figure S3a shows the number of network beads per unit area in contact with the surface when varying the persistence length. When network beads are tightly packed without gaps between them (i.e. each bead covers its projected circular area of 3.14 nm^2 on the surface without free space between projected circular areas), the maximum number of beads per unit area in contact with the surface is 1/3.14 nm^{-2}. The resulting maximum interfacial energy can be expressed as $8.74\varepsilon_A/3.14$ ($k_BT \times nm^{-2}$.) = $11.4\varepsilon_A$ (mJ/m^2). When l_p is larger than 0.244 μm, the interfacial energy decreases when increasing Young's modulus of the network (E), due to decreasing coverage of network beads on the surface. Therefore, the interfacial energy can be estimated as:

$$\gamma_A = \begin{cases} 11.4\varepsilon_A \cdot c_1 & l_p \le 0.024\mu m \\ 11.4\varepsilon_A \cdot c_1 \cdot f(\frac{1}{E}) & l_p > 0.024\mu m \end{cases}, \quad (8)$$

where c_1=0.88 is a corrective constant to account for the gaps between beads on the surface, and $f(1/E)$ is a function of E. The function $f(1/E)$ comes from the fact that density of beads in contact with the surface is inversely proportional to the network Young's modulus, as softer networks are easier to deform and tend to tightly pack at the network-surface interface. When n=4.50, we find that $E \sim l_p^{0.3}$ as shown in Figure S3b. This differs from the scaling law $E \sim l_p$ given in work of V. Negi and R.C. Picu[47]. We should note that they used an athermal finite element model in which fibers are crosslinked rigidly (i.e. crosslinks transmit both force and moment), fiber bending rigidity couples with its Young's modulus, and only changing bending rigidity would not change network volume and mass density, due to the absence of entropic effects. In our model, crosslinks only transmit force, fibril bending rigidity and Young's modulus are independently controlled by two parameters, and only varying the bending rigidity (persistence length) will impact the end-to-end distance of fiber segments as well as the network mass density. Since the exact expression of $f(1/E)$ is unknown, here we choose $f(1/E)=c_3/E$ as a simple approximation, where c_3 is constant with units of Pascal. This model result in the scaling $\gamma_A \sim l_p^{-0.3}$, which can be used to predict the interfacial energy. In Fig. 3(a), the predicted interfacial energy for n=4.50 using this simple model matches with the simulation result. The total strain energy normalized by the interfacial area, γ_C, is equal to the integral of the internal stress (σ) of the network (normal stress perpendicular to the interface) over the displacement (Δl) caused by the pulling force. Its magnitude is equal to multiplying the integration of the internal stress of network over the engineering strain and the initial height of the network. Inspired by the cohesive zone model proposed by Song et. al.[70], in which an exponential form for the free energy potential between the displacement jump and the corresponding traction provides a computationally convenient description of the decohesion process and the cohesive fracture energy is a expression of the peak traction and the critical displacement at peak traction, we normalize the internal stress by the peak value it attains (σ_{max}) and the displacement by the value it takes at the peak stress (d_C). This data is plotted for networks with constant crosslink density but varying persistence length during detachment in Figure S4. Pulling these normalization factors out of the integral, the total strain energy γ_C released during

the detachment can be expressed as $\gamma_C = \sigma_{\max} d_C \int \frac{\sigma}{\sigma_{\max}} d\frac{\Delta l}{d_C}$. It is observed that except networks with a small persistence length (l_p < 0.244 μm), the normalized stress-strain curves collapse onto a master curve as shown in Figure S4. For l_p ≥0.244 μm, $\int \frac{\sigma}{\sigma_{\max}} d\frac{\Delta l}{d_C}$ can be approximated as the area of a triangle $\frac{\sigma_{\max}}{\sigma_{\max}} \cdot \frac{d_C}{d_C} = 1$ as shown in the inserted figure in Figure S4, and then γ_C can be further estimated as $\gamma_C \approx \sigma_{\max} d_C$. This is equivalent to a linear elastic idealization, i.e. $\gamma_C = \sigma_{\max}^2 h / E$, where E is the elastic modulus of the network ad h is the film thickness. At lower persistence lengths, the fit based on modulus will become increasingly inaccurate as entropic effects contribute in addition to purely enthalpic effects. We find that for high persistence lengths, this expression captures the behavior of the strain energy density well. In other words, for l_p < 0.244 μm, $\int \frac{\sigma}{\sigma_{\max}} d\frac{\Delta l}{d_C}$ becomes increasingly less than 1 and cannot be estimated as 1. For networks with constant n=4.50 and varying l_p, simulation results show that the peak stress first increases with decreasing persistence length through a scaling relationship of $\sigma_{max} \sim l_p^{-0.15}$ in the region of l_p ≥0.244 μm, then saturates (Figure S5a). The corresponding displacement at peak stress (d_C) also first increases and then begins to saturate. In the region of l_p ≥0.12 μm, we have $d_C \sim l_p^{-0.225}$ (Figure S5b). Based on $\gamma_C \approx \sigma_{\max} d_C$, $\sigma_{max} \sim l_p^{-0.15}$ and $d_C \sim l_p^{-0.225}$, we can reach a scaling of $\gamma_C \sim l_p^{-0.375}$ in the region of l_p ≥0.12 μm. The absorbed strain energy γ_C predicted by this scaling relationship matches very well with the simulation results in this region as shown in Fig. 3(b). In the region of l_p <0.12 μm, γ_C begins to saturate and $\gamma_C = \sigma_{\max} d_C \int \frac{\sigma}{\sigma_{\max}} d\frac{\Delta l}{d_C}$ is used to give the prediction in Fig. 3(b). Since the interfacial energy (γ_A) and absorbed strain energy (γ_C) mainly contribute to the work of adhesion, superimposition of predicted γ_A and predicted γ_C can be used as the estimation of work of adhesion, γ_T. As displayed in Figure 3(c), the predicted γ_T well captures the dependency of γ_T on the persistence length.

Next, the effect of crosslink density on the work of adhesion is examined. From Figure 3, we can see that when keeping fibril persistence length constant, decreasing crosslink density (n) causes a

very small increase in interfacial energy but a significant increase in the strain energy stored in the network and the work of adhesion. Specifically, when keeping fibril persistence length (l_p=2.44 μm) and adhesive strength (ε_A=1 k_BT) constant, decreasing crosslink density from n=5.47 to n=2.39 leads to a 11% increase in interfacial energy and a very slight decrease in mass density (Figure S6a). The ratio of mean end-to-end distance ($\bar{L}_e$) to the corresponding mean contour length ($\bar{L}_c$) of fibril segments in networks only slightly decreases from 0.98 to 0.96 (Figure S6b). However, a 66% increase in work of adhesion is observed in Figure S6c. Since the change in interfacial energy caused by decreasing n is small, the large increase in work of adhesion is mainly attributed to the change in network stiffness. As shown in Figure S6d, the network with a lower crosslink density is softer (smaller slope of stress-strain curve in the small strain range) but absorbs more strain energy during desorption. A lower crosslink density corresponds to a larger pore size in the network. However, if the number of crosslinks per fibril is lower than a certain threshold value (n≤1.56), the structure is a sparse collection of unconnected subnetworks and is not a robust structure with significant load-bearing capacity as illustrated in Figure S7. In this regime, the network has voids in it that will grow to span the entire cross-section and lead to the disintegration of the network without rupture of the fibrils.

To better understand the desorption process, the instantaneous interfacial energy, strain energy in the network, work of adhesion, and steering force are examined. During desorption, the network experiences a large deformation and polymer density at the interface decreases due to the gradual desorption of fibrils. At the interface, the adhesion between polymer chains and the surface causes a higher polymer density, which is also found at epoxy/Cu interfaces and at the interface between polymer thin films and substrates[69, 71-73]. To detach the network, the applied steering force has to overcome both an interfacial energy barrier and a strain energy barrier. As the network is pulled, the instantaneous interfacial energy decreases while the instant strain energy absorbed by the network and work of adhesion increases until the network fully desorbs (Figure 5 a-c). As shown in Figure 5d, the steering force (the slope of γ_T-Δl curve in Figure 5c) first increases, reaches its maximum value, and then decreases to zero.

To examine how much the interfacial energy contributes to the work of adhesion, we examined the ratio of the work of adhesion to the interfacial energy (γ_T/γ_A). When fixing fibril persistence

length (l_p=2.44 μm) and lowering crosslink density (n), the interfacial energy only slightly increases and the network becomes more flexible (Figure S6d). In this case, γ_T/γ_A monotonically increases from 1.67 to 2.38 (Figure 5e). However, if the network has too few crosslinks to generate sufficient connectivity, the network may also lose structural integrity. Conversely, when fixing network connectivity and decreasing polymer persistence length (0.001 μm ≤ l_p ≤244 μm), the network becomes more flexible and both the interface energy (γ_A) and work of adhesion (γ_T) increase until they reach their plateau values. Interestingly, γ_T/γ_A varies between 1.51 and 2.70, and there is no clear trend for the relationship between γ_T/γ_A and fibril persistence length, as shown in Figure 5f. Without considering entropic effects, greater flexibility of networks induced by smaller polymer persistence length results in a larger γ_T/γ_A. However, decreasing the polymer persistence length should lead to more entropic effects and thermal fluctuations may help desorption. As a result, entropic effects should lead to a decrease in γ_T/γ_A. The multiple regimes in the $\frac{\gamma_T}{\gamma_A}$ $vs.$ l_p curve of Figure 5f suggest that in addition to entropic effects and network stiffness effects, other unknown factors also play roles in determining γ_T/γ_A. Despite the large variation of l_p and n (0.02 μm ≤ l_p ≤244 μm and 2.39 ≤ n ≤ 5.47), γ_T/γ_A varies in a relatively small range (1.51~2.70).

Conclusions

We have developed a coarse-grained model of a crosslinked semiflexible polymer network. Its crosslink density, constituent fibril persistence length (or bending rigidity), and fibril Young's modulus can be independently tuned by varying constants within the bond and angle potentials. The increase in elastic modulus caused by increasing the fibril persistence length leads to a decrease in the interfacial energy, the work of adhesion, and network mass density. Unlike stiff glassy polymer materials, whose interfacial energy is close to the work of adhesion, crosslinked semiflexible polymer networks are able to absorb strain energy during desorption, which greatly contributes to the work of adhesion. Lighter mass density and a corresponding larger pore size are desirable in biopolymer network-based material design. Simulation results show that when considering the effect of network mass density, there is an optimal polymer persistence length that results in a maximum work of adhesion per mass density. When the crosslink density decreases, although the corresponding network mass density and interfacial energy only slightly increase, the

decrease in network elastic modulus allows the network to absorb more strain energy and leads to a profound increase in work of adhesion. However, if the crosslink density is below a certain threshold, networks have no significant load-bearing capacity. Our analysis further reveals that the work of adhesion is about 1.51~2.70 times the interfacial energy across a wide range of fibril persistence length and crosslink density values. While this model uses a coarse-grained fiber as a representation of the curli fiber, a limitation of this approach is that the fiber networks are modeled as chemically crosslinked systems. In reality, curli networks are more appropriately viewed as physically crosslinked or entangled, although they can be modified with mutations to make strong chemical crosslinks as well. While efforts to model physically entangled networks are underway, we use a simpler, crosslinked model to first capture general adhesive behavior of the network. Our findings provide insight into the adhesive mechanisms of biofilm extracellular matrices at the network scale and shed light on the design of biomaterials based on semiflexible polymer networks.

Acknowledgements

This research was sponsored by an award from the Office of Naval Research Young Investigator Program (grant #N00014-15-1-2701). The authors acknowledge a supercomputing grant from the Northwestern University High Performance Computing Center and the Department of Defense Supercomputing Resource Center. E.P.D was additionally sponsored with Government support under and awarded by DoD, Air Force Office of Scientific Research, National Defense Science and Engineering Graduate (NDSEG) Fellowship, 32 CFR 168a. E.P.D. gratefully acknowledges support from the Ryan Fellowship and the Northwestern University International Institute for Nanotechnology.

Reference

1. A. W. Fitzpatrick, S. T. Park and A. H. Zewail, *Proc. Natl. Acad. Sci. USA*, 2013, **110**, 10976-10981.
2. J. F. Smith, T. P. Knowles, C. M. Dobson, C. E. MacPhee and M. E. Welland, *Proc. Natl. Acad. Sci. USA*, 2006, **103**, 15806-15811.
3. T. P. Knowles, A. W. Fitzpatrick, S. Meehan, H. R. Mott, M. Vendruscolo, C. M. Dobson and M. E. Welland, *Science*, 2007, **318**, 1900-1903.
4. T. P. Knowles and M. J. Buehler, *Nat. Nanotechnol.*, 2011, **6**, 469-479.
5. H. Kojima, A. Ishijima and T. Yanagida, *Proc. Natl. Acad. Sci. USA*, 1994, **91**, 12962-12966.

6. Q. Wen and P. A. Janmey, *Curr. Opin. Solid State Mater. Sci.*, 2011, **15**, 177-182.
7. C. Frantz, K. M. Stewart and V. M. Weaver, *J. Cell Sci.*, 2010, **123**, 4195-4200.
8. H.-C. Flemming and J. Wingender, *Nat. Rev. Microbiol.*, 2010, **8**, 623.
9. T. D. Pollard and G. G. Borisy, *Cell*, 2003, **112**, 453-465.
10. C. I. Lacayo, Z. Pincus, M. M. VanDuijn, C. A. Wilson, D. A. Fletcher, F. B. Gertler, A. Mogilner and J. A. Theriot, *PLoS Biol.*, 2007, **5**, e233.
11. L. P. Blanco, M. L. Evans, D. R. Smith, M. P. Badtke and M. R. Chapman, *Trends Microbiol.*, 2012, **20**, 66-73.
12. C. Wu, J. Y. Lim, G. G. Fuller and L. Cegelski, *Biophys. J.*, 2012, **103**, 464-471.
13. T. Kikuchi, Y. Mizunoe, A. Takade, S. Naito and S. i. Yoshida, *Microbiol. Immunol.*, 2005, **49**, 875-884.
14. D. Pawar, M. Rossman and J. Chen, *J. Appl. Microbiol.*, 2005, **99**, 418-425.
15. A. S. Mostaert, R. Crockett, G. Kearn, I. Cherny, E. Gazit, L. C. Serpell and S. P. Jarvis, *Arch. Histol. Cytol.*, 2009, **72**, 199-207.
16. A. S. Mostaert, C. Giordani, R. Crockett, U. Karsten, R. Schumann and S. P. Jarvis, *The Journal of Adhesion*, 2009, **85**, 465-483.
17. A. S. Mostaert, M. J. Higgins, T. Fukuma, F. Rindi and S. P. Jarvis, *J. Biol. Phys.*, 2006, **32**, 393-401.
18. C. Zhong, T. Gurry, A. A. Cheng, J. Downey, Z. Deng, C. M. Stultz and T. K. Lu, *Nat. Nanotechnol.*, 2014, **9**, 858-866.
19. P. Q. Nguyen, Z. Botyanszki, P. K. R. Tay and N. S. Joshi, *Nat. Commun.*, 2014, **5**, 4945.
20. N.-M. Dorval Courchesne, A. Duraj-Thatte, P. K. R. Tay, P. Q. Nguyen and N. S. Joshi, *ACS Biomater. Sci. Eng.*, 2017, **3**, 733-741.
21. C. Noémie-Manuelle Dorval, P. D. Elizabeth, T. Jason, J. K. Jessica, D.-T. Anna, Z. David, K. Sinan and S. J. Neel, *Nanotechnology*, 2018, **29**, 454002.
22. T. P. Knowles and R. Mezzenga, *Adv. Mater.*, 2016, **28**, 6546-6561.
23. N. Lang, M. J. Pereira, Y. Lee, I. Friehs, N. V. Vasilyev, E. N. Feins, K. Ablasser, E. D. O'cearbhaill, C. Xu and A. Fabozzo, *Sci. Transl. Med.*, 2014, **6**, 218ra216-218ra216.
24. J. Li, A. Celiz, J. Yang, Q. Yang, I. Wamala, W. Whyte, B. Seo, N. Vasilyev, J. Vlassak and Z. Suo, *Science*, 2017, **357**, 378-381.
25. C. R. Matos-Pérez, J. D. White and J. J. Wilker, *J. Am. Chem. Soc.*, 2012, **134**, 9498-9505.
26. C. L. Jenkins, H. J. Meredith and J. J. Wilker, *ACS applied materials & interfaces*, 2013, **5**, 5091-5096.
27. M. A. North, C. A. Del Grosso and J. J. Wilker, *ACS applied materials & interfaces*, 2017, **9**, 7866-7872.
28. H. J. Meredith and J. J. Wilker, *Adv. Funct. Mater.*, 2015, **25**, 5057-5065.
29. C. L. Jenkins, H. M. Siebert and J. J. Wilker, *Macromolecules*, 2017, **50**, 561-568.
30. B. P. Lee, P. B. Messersmith, J. N. Israelachvili and J. H. Waite, *Annual review of materials research*, 2011, **41**, 99-132.
31. E. P. DeBenedictis, J. Liu and S. Keten, *Sci. Adv.*, 2016, **2**, e1600998.
32. Y. Zhang, A. Wang, E. P. DeBenedictis and S. Keten, *Nanotechnology*, 2017, **28**, 464002.
33. A. N. Volkov and L. V. Zhigilei, *ACS nano*, 2010, **4**, 6187-6195.
34. Y. Li and M. Kröger, *Carbon*, 2012, **50**, 1793-1806.
35. V. Negi and R. C. Picu, *Journal of the Mechanics and Physics of Solids*, 2019, **122**, 418-434.
36. R. Picu and A. Sengab, *Soft matter*, 2018, **14**, 2254-2266.

37. Z. Qin and M. J. Buehler, *Nat. Commun.*, 2013, **4**, 2187.
38. A. J. Licup, S. Münster, A. Sharma, M. Sheinman, L. M. Jawerth, B. Fabry, D. A. Weitz and F. C. MacKintosh, *Proc. Natl. Acad. Sci. USA*, 2015, **112**, 9573-9578.
39. H. Kang, Q. Wen, P. A. Janmey, J. X. Tang, E. Conti and F. C. MacKintosh, *The Journal of Physical Chemistry B*, 2009, **113**, 3799-3805.
40. C. Storm, J. J. Pastore, F. C. MacKintosh, T. C. Lubensky and P. A. Janmey, *Nature*, 2005, **435**, 191.
41. M. Gardel, J. Shin, F. MacKintosh, L. Mahadevan, P. Matsudaira and D. Weitz, *Science*, 2004, **304**, 1301-1305.
42. F. MacKintosh, J. Käs and P. Janmey, *Phys. Rev. Lett.*, 1995, **75**, 4425.
43. C. P. Broedersz and F. C. MacKintosh, *Reviews of Modern Physics*, 2014, **86**, 995.
44. J. S. Palmer and M. C. Boyce, *Acta Biomater.*, 2008, **4**, 597-612.
45. E. M. Huisman, T. van Dillen, P. R. Onck and E. Van der Giessen, *Phys. Rev. Lett.*, 2007, **99**, 208103.
46. S. Deogekar and R. Picu, *Journal of the Mechanics and Physics of Solids*, 2018, **116**, 1-16.
47. M. Islam and R. Picu, *Journal of Applied Mechanics*, 2018, **85**, 081011.
48. E. Huisman, C. Storm and G. Barkema, *Physical Review E*, 2008, **78**, 051801.
49. E. Huisman, C. Storm and G. Barkema, *Physical Review E*, 2010, **82**, 061902.
50. E. Huisman and T. C. Lubensky, *Phys. Rev. Lett.*, 2011, **106**, 088301.
51. R. J. Pandolfi, L. Edwards, D. Johnston, P. Becich and L. S. Hirst, *Physical Review E*, 2014, **89**, 062602.
52. T. Kim, W. Hwang, H. Lee and R. D. Kamm, *PLoS Comp. Biol.*, 2009, **5**, e1000439.
53. S. Takada, *Curr. Opin. Struct. Biol.*, 2012, **22**, 130-137.
54. M. G. Saunders and G. A. Voth, *Annual review of biophysics*, 2013, **42**, 73-93.
55. Y. Zhang, Z. Meng, X. Qin and S. Keten, *Nanoscale*, 2018, **10**, 4761-4770.
56. L. Ruiz, W. Xia, Z. Meng and S. Keten, *Carbon*, 2015, **82**, 103-115.
57. Y. Zhang, C. Huang, S. Kim, M. Golkaram, M. W. Dixon, L. Tilley, J. Li, S. Zhang and S. Suresh, *Proc. Natl. Acad. Sci. U. S. A.*, 2015, **112**, 6068-6073.
58. E. DeBenedictis, D. Ma and S. Keten, *RSC Advances*, 2017, **7**, 48102-48112.
59. C. W. Jones, J. C. Wang, F. A. Ferrone, R. W. Briehl and M. S. Turner, *Farad. Discuss.*, 2003, **123**, 221-235.
60. C. C. vandenAkker, M. F. Engel, K. P. Velikov, M. Bonn and G. H. Koenderink, *Journal of the American Chemical Society*, 2011, **133**, 18030-18033.
61. M. Schleeger, T. Deckert-Gaudig, V. Deckert, K. P. Velikov, G. Koenderink and M. Bonn, *Polymer*, 2013, **54**, 2473-2488.
62. D. A. Head, A. J. Levine and F. MacKintosh, *Physical review letters*, 2003, **91**, 108102.
63. M. Gardel, J. H. Shin, F. MacKintosh, L. Mahadevan, P. Matsudaira and D. Weitz, *Science*, 2004, **304**, 1301-1305.
64. M. R. Chapman, L. S. Robinson, J. S. Pinkner, R. Roth, J. Heuser, M. Hammar, S. Normark and S. J. Hultgren, *Science*, 2002, **295**, 851-855.
65. X. Wang, D. R. Smith, J. W. Jones and M. R. Chapman, *Journal of Biological Chemistry*, 2007, **282**, 3713-3719.
66. Q. Qi, T.-X. Zhao, B.-L. An, X.-Y. Liu and C. Zhong, *Chinese Chemical Letters*, 2017, **28**, 1062-1068.
67. M. Solar and M. J. Buehler, *Nanotechnology*, 2014, **25**, 105703.
68. S. Plimpton, *Journal of computational physics*, 1995, **117**, 1-19.

69. W. Xia, D. D. Hsu and S. Keten, *Macromolecules*, 2014, **47**, 5286-5294.
70. S. H. Song, G. H. Paulino and W. G. Buttlar, *J. Eng. Mech.*, 2006, **132**, 1215-1223.
71. S. Yang, F. Gao and J. Qu, *Polymer*, 2013, **54**, 5064-5074.
72. S. Yang and J. Qu, *Modell. Simul. Mater. Sci. Eng.*, 2014, **22**, 065011.
73. W. Xia, X. Qin, Y. Zhang, R. Sinko and S. Keten, *Macromolecules*, 2018, **51**, 10304-10311.

Figure legends

Figure 1. Schematic of bead-spring model for semiflexible biopolymers (a), a segment of a coarse-grained biopolymer (b), and a coarse-grained crosslinked network (c).

Figure 2. (a) Schematic of work of adhesion measurement. Steering force *f* is acting on beads on the top layer of network marked by grey color to detach the network from a surface. (b) Representative snapshot of adhesive failure. (c) Representative snapshot of cohesive failure. (d) Work of adhesion (γ_T) as a function of adhesive strength (ε_A), when l_p=2.44 μm and n=4.5.

Figure 3. The effect of fibril persistence length and crosslink density on the interfacial energy (a), the strain energy normalized by the interfacial area stored in the network (b), and the work of adhesion (c).

Figure 4. The effect of crosslink density and fibril persistence length on the interfacial energy γ_A (a), the strain energy per unit interfacial area γ_C absorbed by the network (b), and the work of adhesion γ_T (c) normalized by $\phi_p^{2/3}$, where ϕ_p is the volume fraction of fibrils in the network.

Figure 5. The instantaneous interfacial energy (a), strain energy absorbed by the network (b), work of adhesion (c), and the steering force per unit area (d) as a function of pulling displacement of the steering force (n=4.50 and ε=1 k_BT). γ_T/γ_A as a function of crosslink density (e) and fibril persistence length (f).

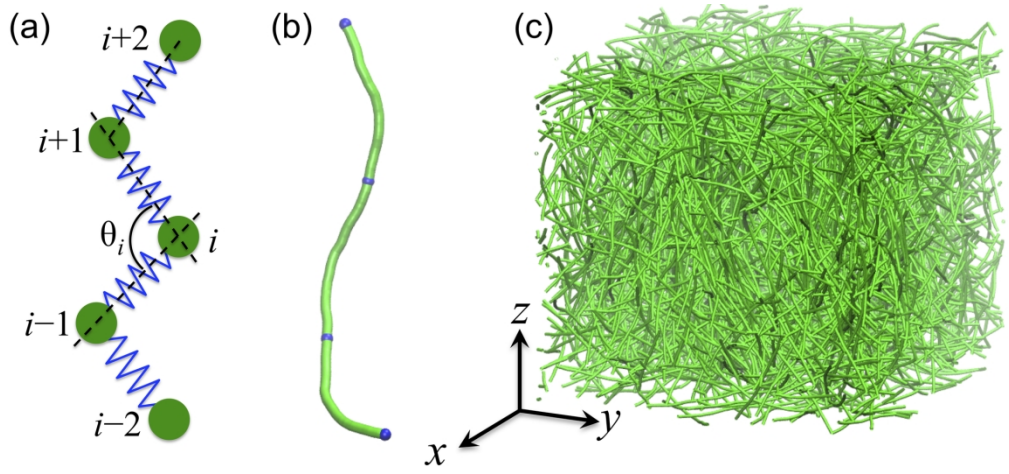

Figure 1. Schematic of bead-spring model for semiflexible biopolymers (a), a segment of a coarse-grained biopolymer (b), and a coarse-grained crosslinked network (c).

184x85mm (300 x 300 DPI)

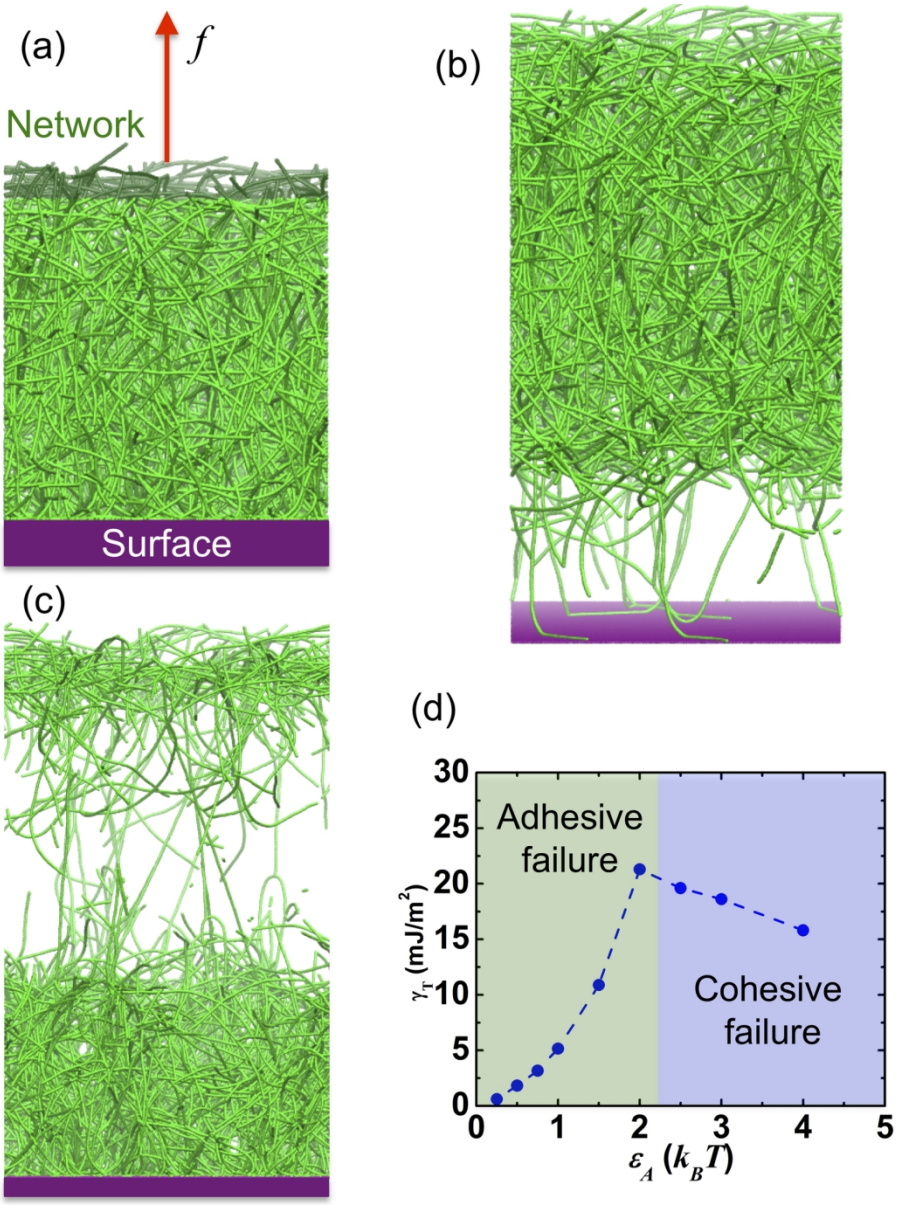

Figure 2. (a) Schematic of work of adhesion measurement. Steering force f is acting on beads on the top layer of network marked by grey color to detach the network from a surface. (b) Representative snapshot of adhesive failure. (c) Representative snapshot of cohesive failure. (d) Work of adhesion (γ_T) as a function of adhesive strength (ε_A), when l_p=2.44 μm and n=4.5.

133x177mm (300 x 300 DPI)

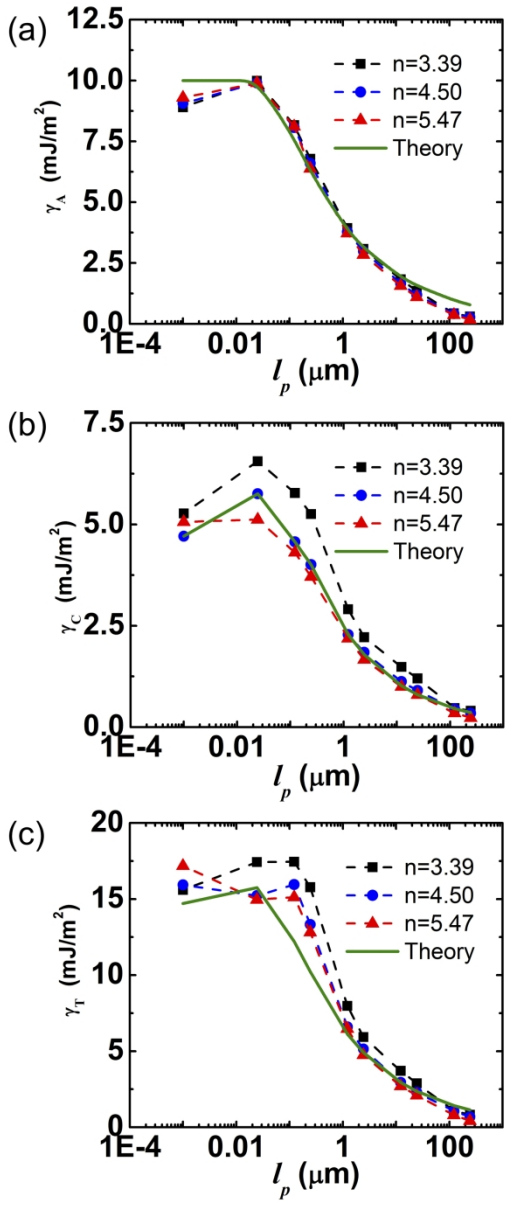

Figure 3. The effect of fibril persistence length and crosslink density on the interfacial energy (a), the strain energy normalized by the interfacial area stored in the network (b), and the work of adhesion (c).

65x155mm (600 x 600 DPI)

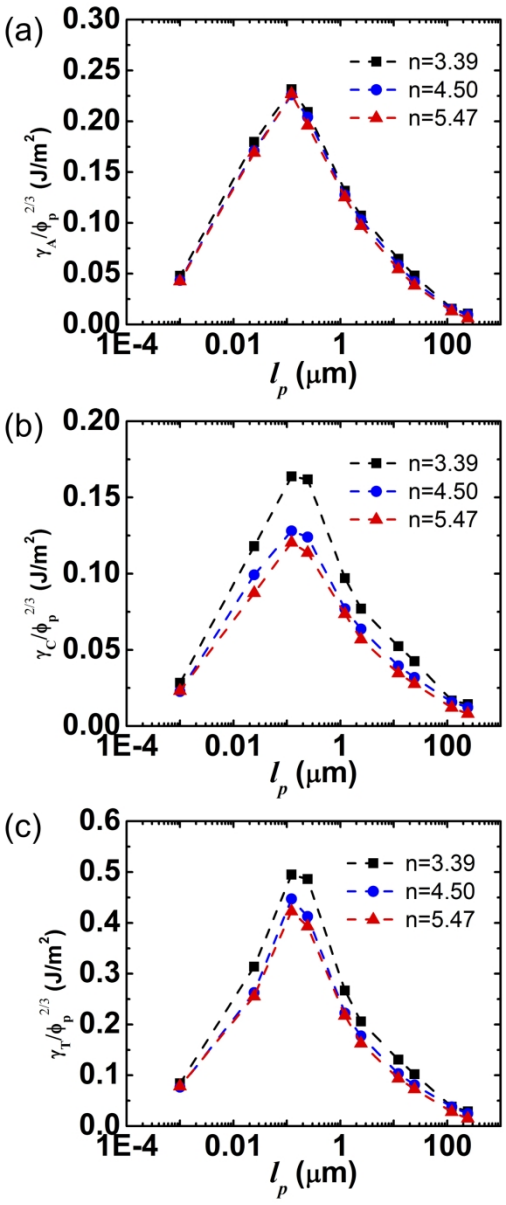

Figure 4. The effect of crosslink density and fibril persistence length on the interfacial energy γ_A (a), the strain energy per unit interfacial area γ_C absorbed by the network (b), and the work of adhesion γ_T (c) normalized by $\phi_p^{2/3}$, where ϕ_p is the volume fraction of fibrils in the network.

65x155mm (600 x 600 DPI)

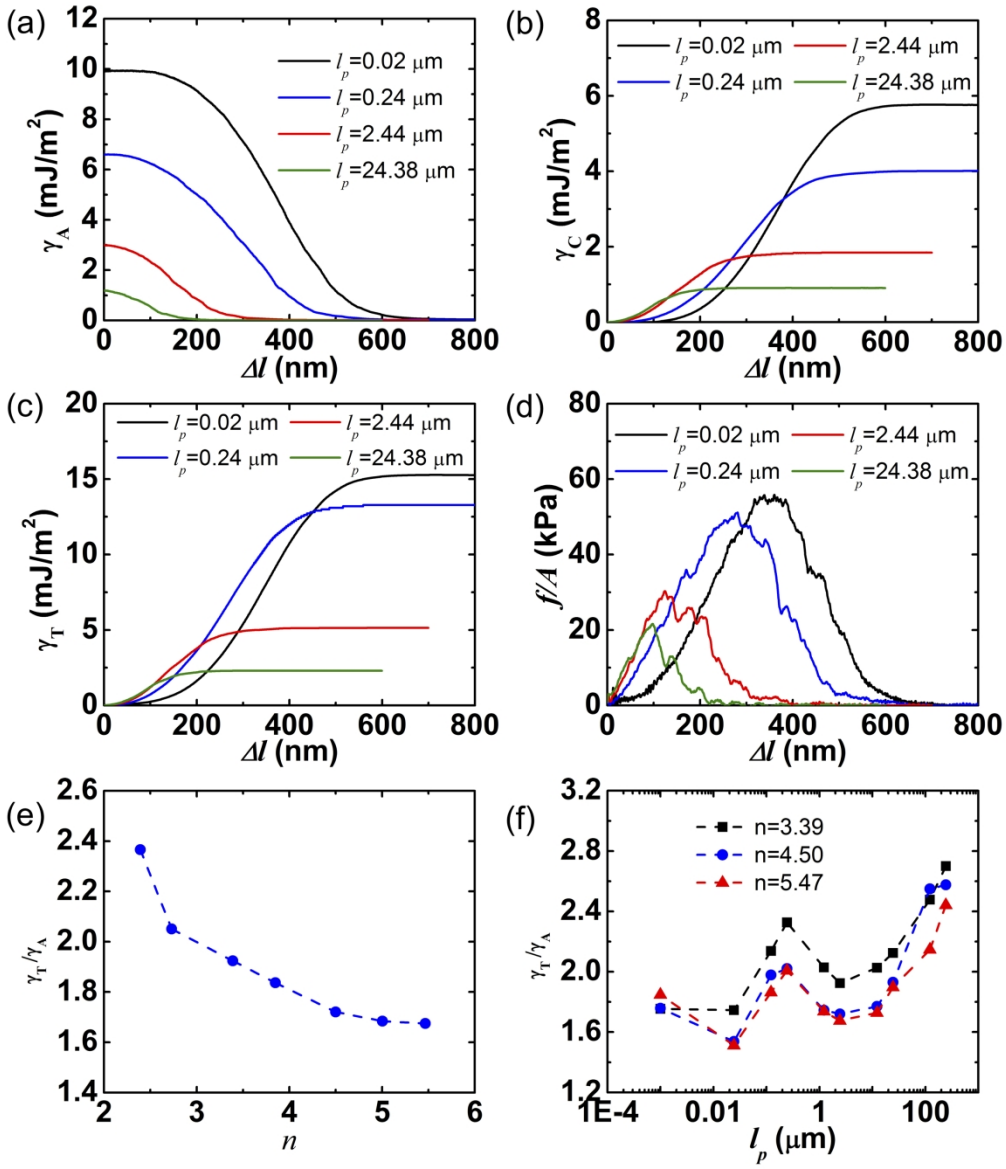

Figure 5. The instantaneous interfacial energy (a), strain energy absorbed by the network (b), work of adhesion (c), and the steering force per unit area (d) as a function of pulling displacement of the steering force (n=4.50 and ε=1 k_BT). γ_T/γ_A as a function of crosslink density (e) and fibril persistence length (f).

130x152mm (600 x 600 DPI)

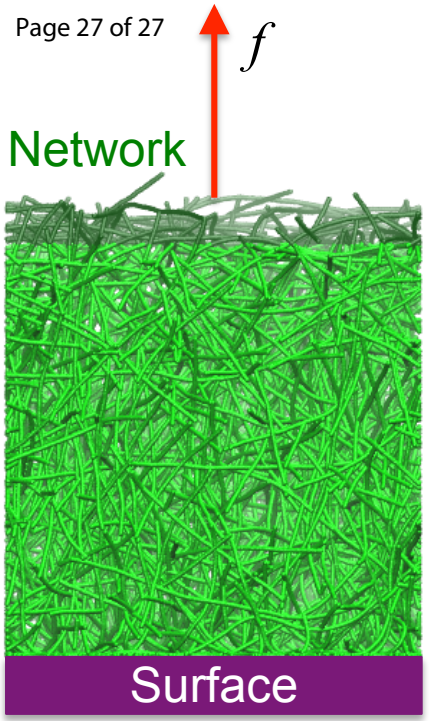
f
Network
Surface

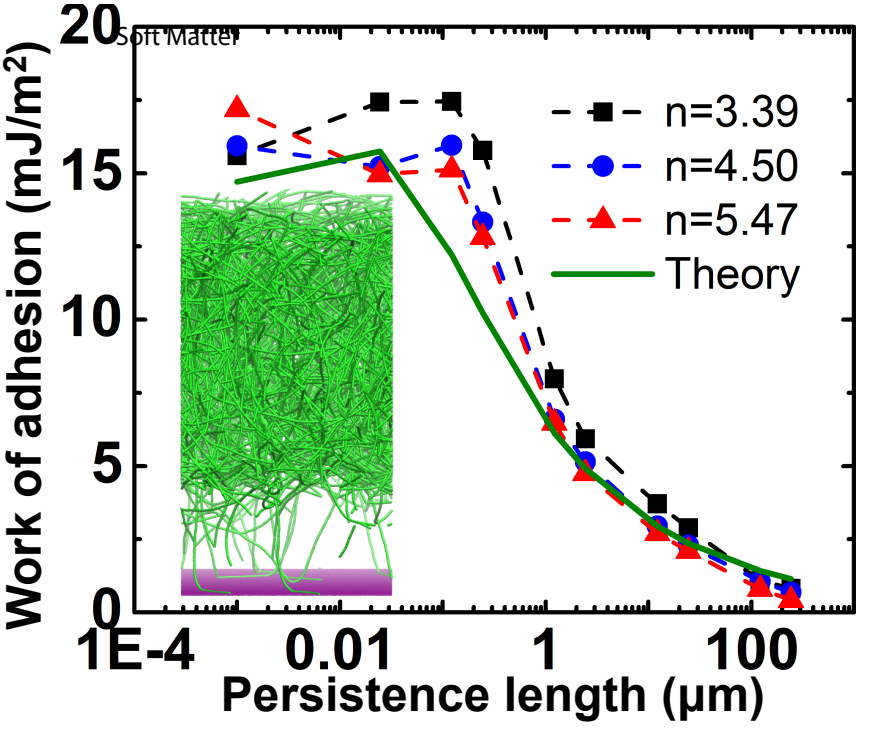
Work of adhesion (mJ/m²)
Persistence length (μm)
1E-4
0.01
1
100
0
5
10
15
20
n=3.39
n=4.50
n=5.47
Theory